CIMAC CONGRESS 25
ZURICH, MAY 19 – 23, 2025

2025 | 456

Effects of methanol-reforming syngas addition on the combustion characteristics of methanol engines

Basic research & advanced engineering - new concepts

Wenju Ma, Harbin Engineering University

La Xiang, Harbin Engineering University
Yu Ding, Harbin Engineering University
Weihe Yao, Harbin Engineering University
Bingquan Li, Harbin Engineering University
Xiaohui Ren, HENAN DIESEL ENGINE INDUSTRY CO.,LTD

ABSTRACT

Methanol, as a low-carbon and easily synthesized fuel, is one of the optimal pathways to achieving great carbon emission reductions in the maritime sector. However, methanol spark-ignition engines suffer from incomplete combustion, resulting in reduced thermal efficiency and increased unconventional emissions. Hydrogen, with its high flame propagation speed and low ignition energy, can promote complete methanol combustion. Due to the challenges of hydrogen storage and transportation, onboard methanol-reforming for hydrogen production presents an effective application strategy in ships. Methanol reforming syngas, however, comprises multiple components including hydrogen, carbon dioxide, and carbon monoxide, making its effects on methanol engine combustion differ from pure hydrogen. In this study, a simulation model for the cylinder of a methanol spark-ignition engine was developed using the CONVERGE simulation platform. Coupled combustion mechanisms for hydrogen-methanol and syngas-methanol mixtures were established to investigate the performance differences between methanol engines fueled by hydrogen and syngas. Additionally, by adjusting syngas composition, the effects of non-standard syngas components on brake-specific fuel consumption (BSFC), NOx emissions, and knock index (KI) under high-load and low-load conditions were analyzed. The results indicate that adding syngas significantly increases the methanol combustion rate, shortens the combustion duration, and enhances the engine's power output capability. However, NOx emissions and KI values are also substantially increased. By increasing the hydrogen proportion in the syngas composition, the formation of CHâ„O radicals at the flame front can be promoted, enhancing methanol oxidation reactions and further improving the engine's power output capability. Consequently, when utilizing methanol reforming syngas on board to enhance methanol engine performance, not only should the blending ratio of syngas be increased, but the hydrogen content in the syngas should also be optimized. This study provides valuable insights into onboard application strategies for the co-combustion of methanol-reforming syngas and methanol, offering guidance for the utilization of methanol-reforming technologies in maritime applications.

1 INTRODUCTION

In recent years, pollutant emissions from ships have become increasingly severe, and traditional diesel fuel, due to its high carbon-to-hydrogen ratio, can no longer meet carbon reduction requirements [1]. Therefore, identifying cleaner and more reliable alternative fuels for the maritime field has become an urgent priority [2]. Among these alternatives, methanol has garnered significant attention due to its complete combustion and clean emissions, making it a promising fuel for achieving deep carbon reduction.

Compared with traditional fuels, methanol fuel molecules do not contain C–C chemical bonds and include an oxygen atom in their molecular structure, enabling more efficient combustion. Methanol exhibits a higher laminar flame speed and octane number, significantly enhancing its anti-knock performance and isochoric combustion ratio. When combined with a high compression ratio, these characteristics enable higher combustion thermal efficiency. Additionally, methanol has a lower adiabatic flame temperature, which not only reduces heat transfer losses but also helps suppress the formation of nitrogen oxides (NOx) due to the lower flame temperature [3,4].

Currently, technologies such as high compression ratios, in-cylinder direct injection, and exhaust gas recirculation (EGR) have become common methods to improve methanol combustion characteristics and reduce emissions. Panagiotis Karvounis [5] investigated the differences between methanol port fuel injection and in-cylinder direct injection in a methanol/diesel dual-fuel engine. The results showed that methanol direct injection can achieve up to 95% methanol energy substitution while maintaining knock-free combustion conditions and simultaneously reducing NOx emissions by 85%. As the methanol energy ratio increases, the indicated thermal efficiency of the methanol direct injection engine improves. Yanju Wei [6] explored the effects of three different EGR technologies on methanol engine performance. EGR effectively reduces the in-cylinder temperature during the compression stroke, suppressing the knocking tendency in spark-ignition methanol engines. Hao Feng [7], leveraging methanol's high octane number and high latent heat of vaporization, investigated the potential of high compression ratios to improve engine performance. The study revealed that for spark-ignition methanol engines, increasing the compression ratio from 11.5 to 15.3 results in improved fuel economy under stoichiometric combustion conditions. However, due to methanol's high latent heat of vaporization, methanol engines often face starting difficulties and experience deteriorated combustion performance at low loads, leading to significant unburned hydrocarbon emissions [8,9]. However, existing research indicates that methanol engines are more prone to knocking phenomena under full-load conditions[10,11].

Hydrogen blending with methanol is one of the promising technological pathways to address the afore-mentioned challenges. Combined hydrogen's high flame propagation speed, short quenching distance, and low ignition energy, a more consistent combustion process and higher thermal efficiency can be achieved [12,13]. S.N. Iyer [14] investigated the effect of hydrogen addition on a direct-injection spark-ignition methanol engine. The results revealed that hydrogen addition increased hydroxyl radical concentrations, shortened combustion duration, and reduced CO and soot emissions. Moreover, hydrogen enrichment extended the latest possible injection timing for methanol, enabling better fuel-air mixing and more effective combustion control. Zhi Tian [15] developed an alcohol-H_2 engine model and conducted a comparative analysis of the combustion and emission performance of methanol-H_2, ethanol-H_2, and n-butanol-H_2 blends. Compared to ethanol-H_2 and n-butanol-H_2 blends, the methanol-H_2 blend at 2000 rpm reduced CO emissions by 48.28% and 65.91%, and CO_2 emissions by 14.9% and 24.61%, respectively. A higher hydrogen blending ratio was shown to improve brake torque, reduce BSFC, and lower carbon emissions. Changming Gong [16] studied hydrogen blending and methanol injection strategies in a dual-fuel engine equipped with hydrogen port injection and methanol direct injection systems. The results demonstrated that hydrogen addition extended the lean-burn limit of the methanol engine from an equivalence ratio of 1.6 to 2.2. Hydrogen addition also shortened the flame development angle and rapid combustion angle, bringing the combustion center closer to the top dead center. Therefore, adding hydrogen to methanol engines can significantly enhance the in-cylinder flame propagation of methanol, resulting in higher brake torque and lower BSFC, while also reducing the engine's carbon emissions.

On the other hand, although hydrogen significantly improves methanol combustion and reduces emissions, its stringent storage and transportation requirements pose substantial challenges for practical applications. Therefore, researchers have proposed the concept of on-board methanol reforming to produce hydrogen. Methanol steam reforming offers high hydrogen yield, operates under mild reaction conditions, and can effectively utilize engine exhaust heat, making it highly suitable for practical applications. Cheng-Hsun Liao [17] investigated a methanol reformer that

utilizes engine exhaust heat combined with methanol steam reforming (MSR) to produce hydrogen. The results showed that under high engine load conditions, with a throttle opening set at 20%, the exhaust temperature and heat flow were sufficient to sustain MSR. When the steam-to-carbon ratio was set to 1.2 and the methanol supply rate was fixed at 15.8 g/min, the methanol conversion efficiency approached 93%, and hydrogen production remained stable at approximately 75%. The molar rate of hydrogen was around 1.34 mol/min, and the hydrogen yield per unit of exhaust heat was 1.6 mol/MJ. Alankrit Srivastava [18] employed a packed-bed reactor to investigate the performance of a reformer utilizing exhaust heat to sustain the reforming reaction. The results indicated that temperature was the most influential inlet parameter, while increasing the reactant inlet flow rate significantly reduced methanol conversion efficiency due to the shortened residence time in the catalyst zone for the reforming reaction.

The syngas obtained from methanol steam reforming typically consists of 75% hydrogen and 25% carbon dioxide. Additionally, due to the incomplete reforming reaction, trace amounts of carbon monoxide are also produced. Therefore, the effects of syngas and pure hydrogen on the combustion and emission characteristics of methanol engines are not entirely identical. Haochen Zhan [19] conducted experiments on methanol pyrolysis and methanol-syngas oxidation using a flow reactor under pressures ranging from 1.0 to 5.0 MPa. The results indicated that high pressure slightly promoted methanol pyrolysis while reducing formaldehyde formation. Syngas inhibited methanol oxidation and decreased formaldehyde generation. Kinetic analysis revealed that the effect of blending ratios on methanol-syngas co-oxidation could be categorized into dilution effects and chemical effects. Yongjian Wang [20] developed a chemical mechanism for hydrogen-methanol and methanol-cracked syngas-methanol combustion, quantitatively analyzing the impact of hydrogen and syngas on methanol engine performance. The results showed that within the knock limit, the syngas blending ratio could reach up to 0.076. Compared to a pure methanol engine, the system's overall thermal efficiency increased by 1.96%. These studies play a significant role in advancing the understanding of methanol-syngas co-oxidation reactions and syngas/methanol in-cylinder combustion processes.

The aforementioned studies demonstrate that methanol is a promising fuel for achieving carbon reduction in the maritime sector. However, methanol engines still face challenges such as incomplete combustion under low-load conditions and knocking issues under high-loads conditions. The hydrogen-rich syngas produced via methanol steam reforming effectively improves in-cylinder combustion in methanol engines, achieving higher thermal efficiency while addressing the hydrogen storage and transportation challenges in maritime applications. Current research primarily focuses on the effects of pure hydrogen on methanol engine combustion and emissions. However, the stringent requirements for hydrogen storage and transportation significantly limit its practical application onboard ships. Moreover, syngas and hydrogen differ considerably in composition, leading to variations in their impact on methanol engine combustion and emission characteristics. The specific effects of syngas on methanol engines remain insufficiently understood. Although some researchers have begun exploring the differences between the effects of syngas and hydrogen on methanol engines, most studies focus on standard syngas compositions, neglecting the impact of non-standard syngas compositions on spark-ignited methanol engines.

In this study, a computational fluid dynamics simulation model of a spark-ignited methanol engine cylinder was established. Key performance parameters, including knock index (KI), BSFC, indicated mean effective pressure (IMEP), and NOx emissions, were analyzed to investigate the effects of standard syngas compositions on combustion and emission performance. Building on this foundation, three different H_2/CO_2 ratios for reformate gas were set to explore the effects of non-standard syngas compositions on the performance of the spark-ignited methanol engine. Additionally, the differences between hydrogen and reformate gas on methanol engine combustion and emissions were compared. Finally, considering varying engine load requirements, parameter studies were conducted under both high and low load conditions to provide a comprehensive understanding of the effects of syngas blending on spark-ignited methanol engines.

The innovations of this study are as follows: (a) The differences in the effects of methanol reforming syngas and hydrogen on spark-ignited methanol engine performance were investigated. (b) The impact of non-standard syngas compositions on spark-ignited methanol engines was explored. In practical maritime applications, in addition to increasing the blending ratio, combustion performance can also be optimized by adjusting the syngas composition.

2 METHODOLOGIES

This study is based on a spark-ignited methanol engine. In this section, a CFD model of the engine

cylinder was established considering the specific characteristics of the methanol engine, and the model was validated using experimental data.

2.1 Engine Modeling Principles

The methanol engine simulation model was established using the CONVERGE simulation software platform. This platform is equipped with autonomous mesh generation, advanced physical models, high-level chemical solvers, and exceptional capabilities for handling complex moving geometries [21]. In CONVERGE, fluid flow dynamics are governed by equations describing the conservation of mass, momentum, and energy. Additional equations represent turbulence, passive scalars, and species transport. The compressible forms of the mass, momentum, and energy transport equations are as follows:

$$\frac{\partial \rho}{\partial t} + \frac{\partial \rho u_i}{\partial x_i} = S \tag{1}$$

$$\frac{\partial \rho u_i}{\partial t} + \frac{\partial \rho u_i u_j}{\partial x_j} = -\frac{\partial P}{\partial x_i} + \frac{\partial \sigma_{ij}}{\partial x_j} + S_i \tag{2}$$

$$\begin{aligned} &\frac{\partial \rho e}{\partial t} + \frac{\partial u_j \rho e}{\partial x_j} = -P\frac{\partial u_j}{\partial x_i} + \sigma_{ij}\frac{\partial u_i}{\partial x_j} \\ &+ \frac{\partial}{\partial x_j}\left(K\frac{\partial T}{\partial x_j}\right) + \frac{\partial}{\partial x_j}\left(\rho D\sum_m h_m \frac{\partial \gamma_m}{\partial x_j}\right) + S \end{aligned} \tag{3}$$

Where, ρ represents the density, u denotes the velocity, S is the source term, P stands for the pressure, σ_{ij} represents the stress tensor, e refers to the specific internal energy, K is the thermal conductivity, D represents the mass diffusion coefficient, h denotes the enthalpy, γ_m refers to the mass fraction of species m.

The Redlich-Kwong equation of state [22] is used to characterize the working fluid conditions inside the cylinder.

$$p = \frac{RT}{V-b} - \frac{a}{V^2 + ubV + wb^2} \tag{4}$$

Where, p represents the pressure, R denotes the gas constant, T stands for the temperature, V is the volume, b, a, u, w are the Redlich-Kwong coefficients.

Table 1 presents the selected mathematical models and chemical mechanisms, along with brief descriptions of their contents. The SAGE model was chosen to simulate the combustion process, while detailed chemical kinetics were described using the ARAOP mechanism [20], which includes 39 species and 193 reactions. NOx emissions were calculated using the extended Zeldovich mechanism. In addition, the RNG k-ε model and the O'Rourke-Amsden model were employed to characterize in-cylinder turbulence and heat transfer, respectively.

Table 1. Employed mathematical models and chemical mechanisms in the 3D CFD simulation model.

Models/ mechanism	Sub-model	Brief introduction
Combustion	SAGE model	SAGE calculates the reaction rates for each elementary reaction while the CFD solver solves the transport equations.
Reaction kinetics	ARAOP mechanism	The mechanism includes 39 species and 193 reactions. The influence of CO and H_2 on the combustion of methanol was considered.
Turbulence	RNG k-ε model	The Renormalization Group (RNG) k-ε turbulence model shows better performance in characterising anisotropic and non-equilibrium effect than the standard k-ε turbulence model.
NOx formation	Extended Zeldovich mechanism	A third reaction accounting for the OH radicals influence is supplemented to the two reaction sproposed by Zeldovich, which evaluate the NO formation from atmospheric nitrogen and oxygen.
Heat transfer	O'Rourke-Amsden model	The molecular conductivity, Prandtl number, fluid temperature, wall temperature and shear speed are used for evaluating the heat transfer.

2.2 Model Setup

The research focuses on a spark-ignited methanol engine with a rated speed of 1500 r/min and a rated power of 320 kW. The engine adopts a V-type configuration, and methanol is injected via the port fuel injection method. The key engine parameters are presented in Table 2.

Table 2. Engine main characteristics.

Parameter	Unit	Value
Bore	mm	128
Stroke	mm	140
Nominal Engine Speed	r/min	1500
Nominal power	kW	320
Compression Ratio	-	12
Number of cylinders	-	8

A complete three-dimensional geometric model was established based on the actual combustion chamber and cylinder head profile of the methanol

engine. This model was then imported into CONVERGE Studio to configure initial conditions, boundary conditions, ignition models, combustion models, and emission models. The developed 3D CFD model simulates the process from Intake Valve Closure (IVC) to Exhaust Valve Opening (EVO). The computational domain at the IVC point is shown in Figure 1.

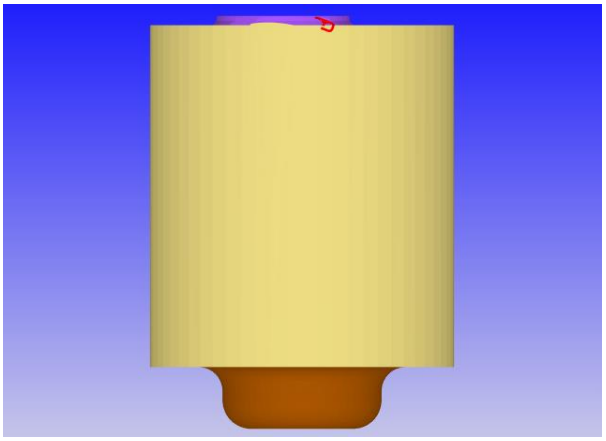

(a) Three-dimensional geometric cross-sectional view of the cylinder model

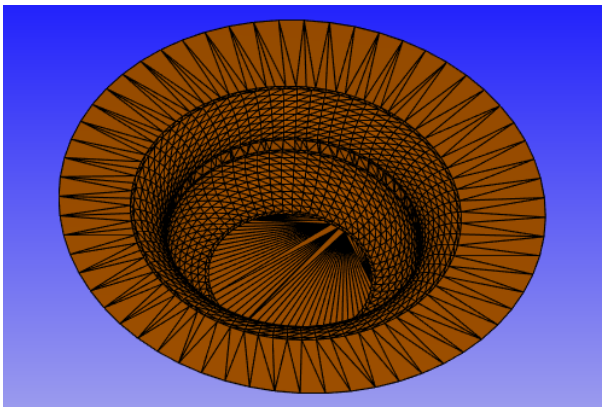

(b) The combustion chamber model of the engine

Figure 1. Three-dimensional cylinder model of a methanol engine.

In this study, CONVERGE software was utilized with its base grid size, Adaptive Mesh Refinement (AMR), and fixed mesh refinement strategies for grid control. The initial grid size was set to 3.5 mm, and two adaptive mesh control strategies—velocity-based refinement and temperature-based refinement—were employed to address the rapid changes in temperature and velocity during combustion. For velocity-based adaptive mesh refinement, the maximum embedding level and sub-grid criterion were set to 2 and 2.0 m/s, respectively. For temperature-based adaptive mesh refinement, the maximum embedding level and sub-grid criterion were set to 2 and 5.0 K, respectively. Additionally, to prevent numerical divergence in the spark ignition source region, a two-level spherical fixed refinement strategy was applied, with levels 4 and 5 specified around the spark plug ignition source. The fixed mesh refinement around the spark plug is shown in Figure 2.

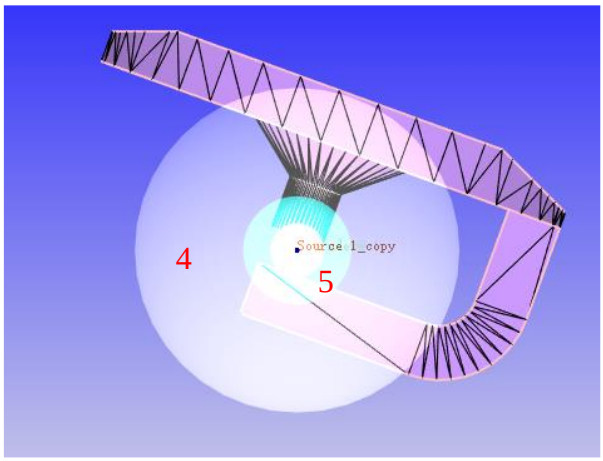

Figure 2. Dense fixed grid around the spark plug.

Figure 3 illustrates the spark plug ignition energy release pattern under 100% load conditions. The total ignition energy is 0.02 J, which is divided into two distinct phases, each contributing 0.01 J. The first phase represents the rapid energy release period, lasting for 0.5° CA. The second phase corresponds to the sustained energy release period, with an ignition duration of 10° CA.

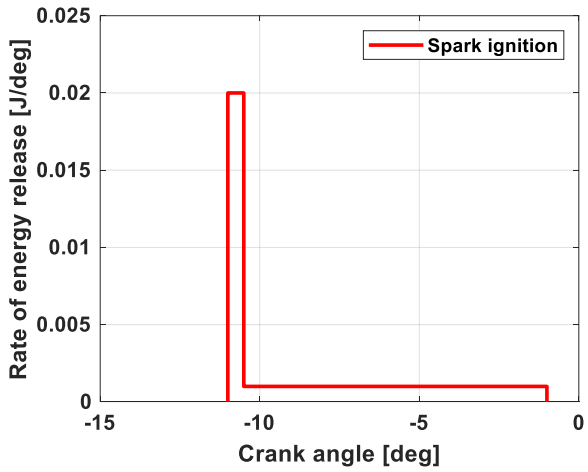

Figure 3. Spark plug ignition timing.

To detect potential knock phenomena within the combustion chamber, this study utilized the Central Composite Design (CCD) theory from experimental design. A total of 13 monitoring points were evenly distributed on the XY plane to monitor local pressure fluctuations, enabling rapid detection of

abnormal in-cylinder pressure oscillations caused by factors such as end-gas autoignition. The knock pressure monitoring points are categorized into three types: one central point (yellow), eight axial points (red), and four quadrant points (blue). The specific arrangement of these monitoring points, referenced to the cylinder wall, is shown in Figure 4.

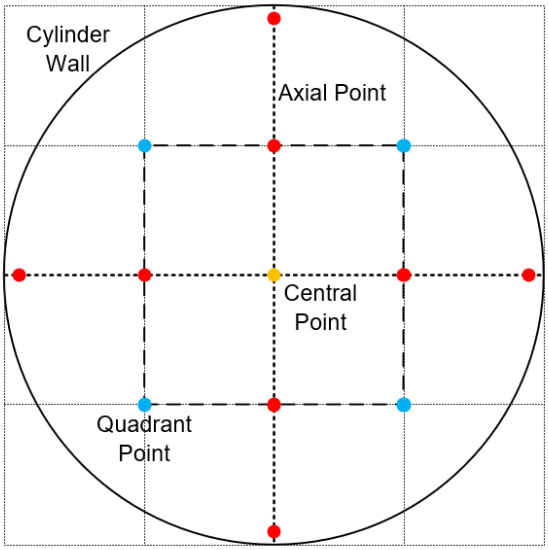

Figure 4. Knock monitoring point configuration.

The Knock Index (KI) is introduced to define the intensity of knock and is used to quantify the knocking phenomenon. The definition of KI is given by Equation (5).

$$KI = \frac{1}{N}\sum_{1}^{N} PP_{\max,n} \tag{5}$$

Where, $PP_{\max,n}$ represents the maximum absolute difference of the band-pass filtered pressure (5 kHz–20 kHz) at location n.

The base grid size significantly affects both the computational speed and prediction accuracy of the CFD model. To eliminate the influence of grid size, in-cylinder pressure was calculated under rated operating conditions using four grid sizes: 3.5 mm, 3 mm, 2.5 mm, and 2 mm, as shown in Figure 5. The pressure curve of Grid 3 (2.5 mm) closely matched that of Grid 4 (2 mm), while noticeable differences were observed compared to Grid 1 (3.5 mm) and Grid 2 (3 mm). Considering both computational cost and prediction accuracy, Grid 3 (2.5 mm) was selected as the base grid size for subsequent research.

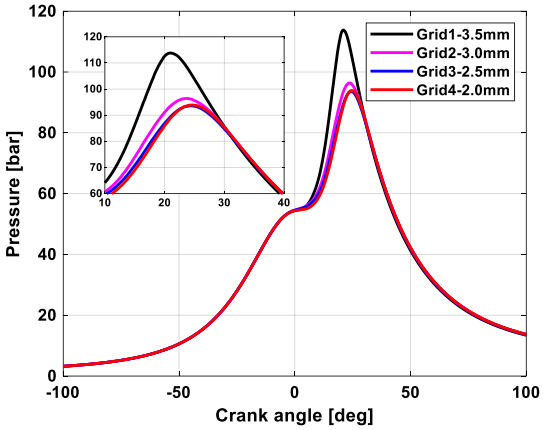

Figure 5. In-cylinder pressure comparison with four mesh sizes.

2.3 Model Validation

Considering that this study primarily focuses on high-load and low-load conditions of the methanol engine, simulations were conducted under 100% load and 25% load based on the modeling theories and methods. The CFD cylinder model was validated against experimental data for methanol engine performance, including BSFC, IMEP, NOx emissions, effective output power, and cumulative heat release under these two operating conditions. This validation ensures that the model achieves a high degree of accuracy.

Figure 6 shows the comparison between experimental results and simulation results under different operating conditions. Figure 6(a) and Figure 6(c) compare the cumulative heat release results from simulations and experiments for methanol combustion under 100% load and 25% load conditions. During the study, the experimental results of CA5, CA10, CA50, and CA90 heat release points were analyzed. Figure 6(b) and Figure 6(d) present the in-cylinder pressure and heat release rate results obtained from the CFD model under 100% load and 25% load conditions. At 100% load, the maximum cylinder pressure was 92.88 bar, with the maximum peak pressure angle occurring at 23.74° CA, compared to an experimental value of 19.56° CA. The maximum heat release rate reached 552.89 J/°CA, and the total combustion duration spanned 56° CA. At 25% load, the maximum cylinder pressure was 24.10 bar, with the maximum peak pressure angle occurring at 22.78° CA, compared to an experimental value of 17.69° CA. The maximum heat release rate was 110.61 J/°CA, and the total combustion duration extended to 82° CA.

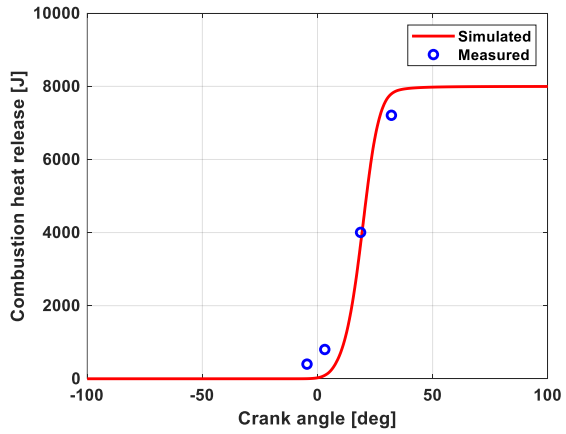

(a) Combustion heat release at 100% load condition.

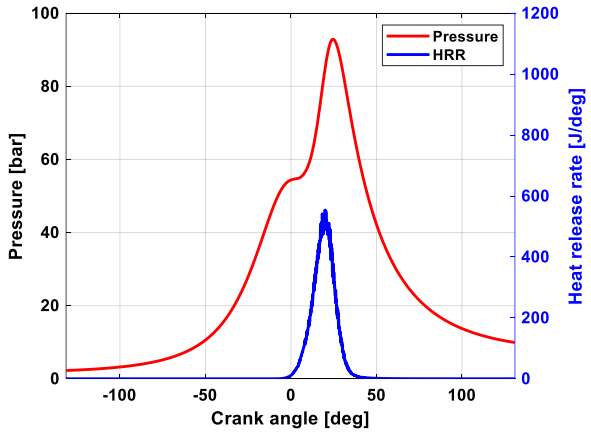

(b) Pressure and heat release rate at 100% load condition.

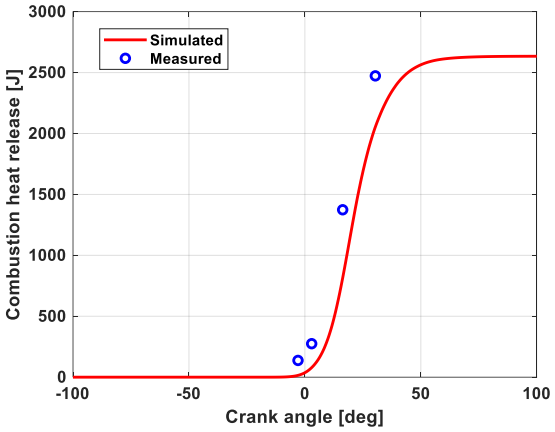

(c) Combustion heat release at 25% load condition.

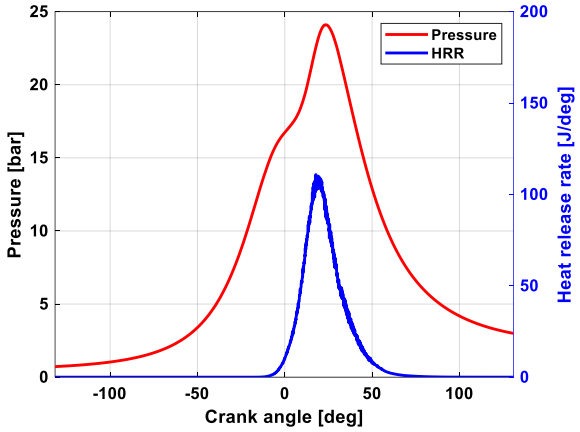

(d) Pressure and heat release rate at 25% load condition.

Figure 6. Comparison between simulation results and experimental results.

Table 3 presents the comparison between simulation results and experimental results of the methanol engine cylinder model under different operating conditions. In this study, the engine simulation model was validated using six key parameters obtained from methanol engine bench tests: maximum peak pressure angle (p_{max} angle), IMEP, output power, BSFC, thermal efficiency, and NOx emissions. The maximum relative error to the experimental values (Error.exp) for IMEP, Power, BSFC, and Thermal Efficiency was 4.84%, which satisfies the acceptable engineering research error margin of 5%. The mechanical efficiency of the methanol engine is 0.87 at 100% load and 0.75 at 25% load. The Error.exp for NOx emissions was 9.58%. Considering that the NOx emission model is inherently predictive and typically exhibits larger discrepancies in simulation studies, the error can be considered acceptable. Therefore, based on the comparisons shown in Figure 6 and Table 3, it can be concluded that the established methanol engine model demonstrates high accuracy under both 100% load and 25% load conditions, providing a reliable foundation for subsequent research.

Table 3. Comparison of simulation and experimental results for methanol engine cylinder model under different operating conditions.

Operation loads	Parameters	p_{max} angle	IMEP	Power	BSFC	Thermal efficiency	NOx
	Unit	°CA	bar	kW	g/(kW·h)	%	g/(kW·h)
100% load	Simulation	23.74	20.39	319.56	427.00	43.08	2.63
	Experiment	19.56	20.57	320.06	440.01	41.81	2.40
	Error.exp (% or °CA)	4.18	0.88	0.16	2.96	3.04	9.58
25% load	Simulation	22.78	6.09	82.20	548.40	33.55	1.48
	Experiment	17.69	6.40	81.74	551.55	33.35	1.51
	Error.exp (% or °CA)	5.09	4.84	0.56	0.57	0.60	1.99

3 RESULTS AND ANALYSIS

This section first investigates the impact of standard syngas composition on the combustion process and power performance parameters of the methanol engine. Subsequently, the effects of non-standard syngas on the performance of the methanol engine were investigated by increasing the hydrogen content in the syngas. Based on this, the changes in methanol engine performance were analyzed for BSFC, NOx emissions, and KI, considering the influence of syngas addtion and hydrogen addition, as well as the hydrogen percentage variation in the syngas.

The validated CFD model was employed to investigate the effects of methanol reforming syngas on engine knock, combustion, and emission performance. To highlight the distinct characteristics of high-load and low-load operation in methanol engines, the study was conducted under 100% load and 25% load conditions. The standard composition of methanol reforming syngas used in this study is shown in Table 4.

Table 4. Standard methanol reforming syngas composition.

Parameter	Unit	Volume fraction
H_2	%	73
CO	%	2
CO_2	%	25

There are significant differences in the volumetric heating value and mass-specific heating value between methanol fuel and syngas. Using volume-based blending ratios or mass-based blending ratios would inevitably lead to substantial variations in the total energy input into the combustion chamber. Therefore, to more intuitively represent the impact of syngas composition on methanol combustion and emission performance, this study adopts an energy-based blending ratio approach. This method ensures that the total energy released from the fuel remains constant before and after blending. The energy-based blending ratio formula is expressed as Equation(6).

$$\varepsilon = \frac{m_{sg} LHV_{sg}}{m_M LHV_M + m_{sg} LHV_{sg}} \tag{6}$$

Where, ε represents the energy blending ratio of syngas, m denotes the fuel mass, LHV refers to the Lower Heating Value of the fuel, Subscripts M and sg represent methanol and syngas, respectively.

3.1 The Effect of Syngas on Spark-Ignition Methanol Engine

To clarify the impact of syngas blending ratios on the combustion process and performance of methanol engines, this study conducted simulations with syngas blending ratios of 5%, 10%, and 15% mixed with methanol. The simulation results are shown in Figure 7. From Figure 7(a), Figure 7(b), and Figure 7(c), it can be inferred that as the syngas blending ratio increases, the in-cylinder pressure, maximum heat release rate, and in-cylinder combustion temperature all increase. Syngas effectively accelerates the combustion speed of methanol, shortening the duration of the heat release process. Additionally, based on the heat release rate and in-cylinder temperature, it can be observed that syngas has a minimal effect on the ignition phase of the methanol engine. Its primary impact occurs during the combustion development phase. This is mainly because the proportion of syngas in the working medium is relatively low, and the ignition process in the cylinder remains dominated by methanol fuel.

Figure 7(d) shows the mass fraction variation of CH_2O radicals under different syngas blending ratios. CH_2O radicals are primarily distributed at the flame front and serve as precursors for oxidation reactions in engines [23]. From Figure 7(d), it can be seen that the addition of syngas significantly increases the formation of CH_2O radicals. However, as the syngas blending ratio continues to rise, the growth rate of CH_2O radical mass fraction slows down, indicating that the components in syngas can induce or promote methanol oxidation reactions, but this promotion effect plateaus beyond a certain syngas blending ratio. The formation process of CH_2O radicals in the cylinder is shown in Figure 8. It can be observed that with the addition of syngas, the oxidation process of methanol in the cylinder proceeds faster, and the duration of the oxidation process shortens.

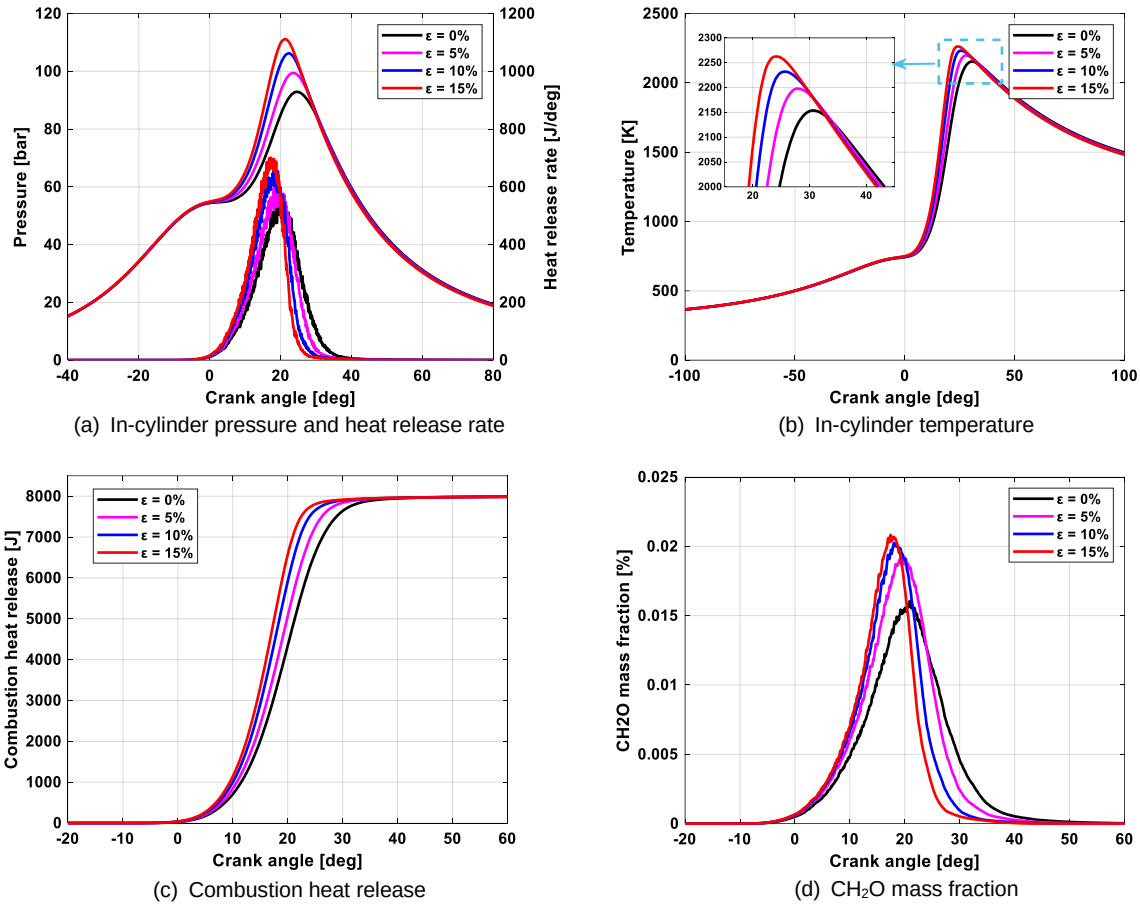

(a) In-cylinder pressure and heat release rate

(b) In-cylinder temperature

(c) Combustion heat release

(d) CH_2O mass fraction

Figure 7. Simulation results with syngas blending ration variation.

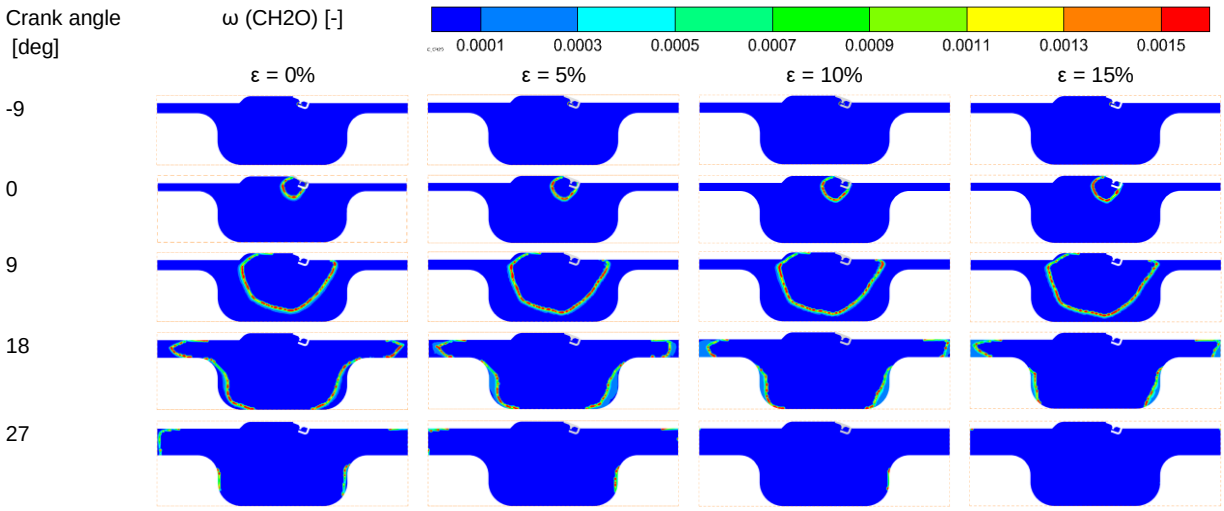

Figure 8. In-cylinder CH_2O distribution with syngas blending ration variation.

Figure 9 illustrates the effects of standard syngas composition addition on the work output and emission performance of a spark-ignited methanol engine. Figure 9 (a) shows the changes in the air-fuel ratio (AFR) and equivalence ratio (λ) of the in-cylinder mixture with increasing syngas blending ratios. As the blending ratio increases, the air-fuel ratio gradually decreases, while the equivalence ratio significantly rises. This trend is primarily due to hydrogen's high mass-specific lower heating value and high theoretical air-fuel ratio in the syngas composition. Figure 9(b) and Figure 9(c) present the variation in KI, IMEP, and BSFC with increasing syngas blending ratios. The simulation results indicate that higher syngas blending ratios result in a higher IMEP, enabling the engine to

achieve greater power output and lower BSFC. However, the KI also increases significantly, indicating a stronger tendency for engine knock.

Figure 9(d) displays the changes in NOx and CO_2 specific emissions. Here, only direct CO_2 emissions from the methanol engine are considered. The results show that syngas addition reduces CO_2-specific emissions, thereby lowering the engine's carbon footprint. However, NOx emissions increase substantially. This is mainly due to the formation of high-temperature regions closer to the top dead center (TDC), as shown in Figure 10. With increasing syngas blending ratios, the in-cylinder temperature rises, and the high-temperature zone shifts closer to TDC, leading to a significant increase in NOx formation.

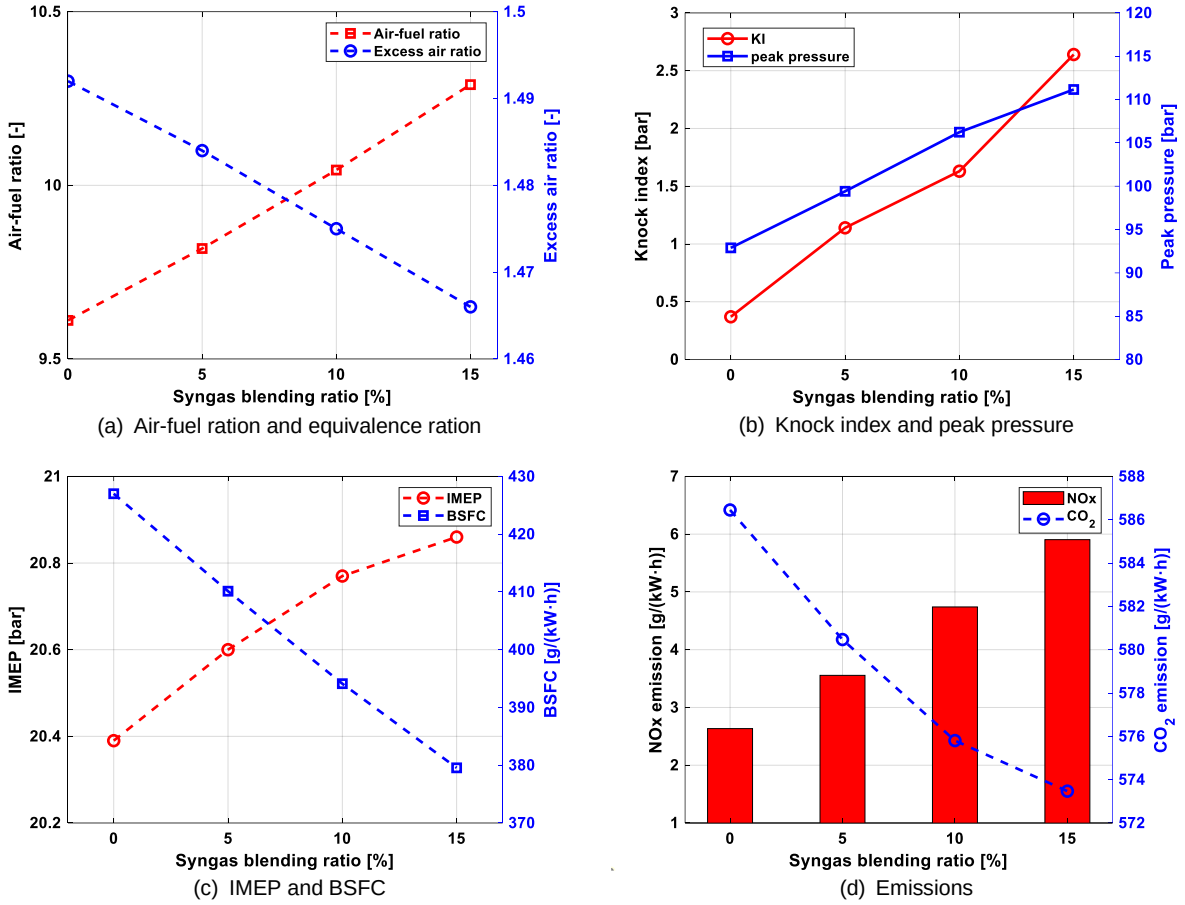

(a) Air-fuel ration and equivalence ration

(b) Knock index and peak pressure

(c) IMEP and BSFC

(d) Emissions

Figure 9. Simulation results with syngas blending ration variation.

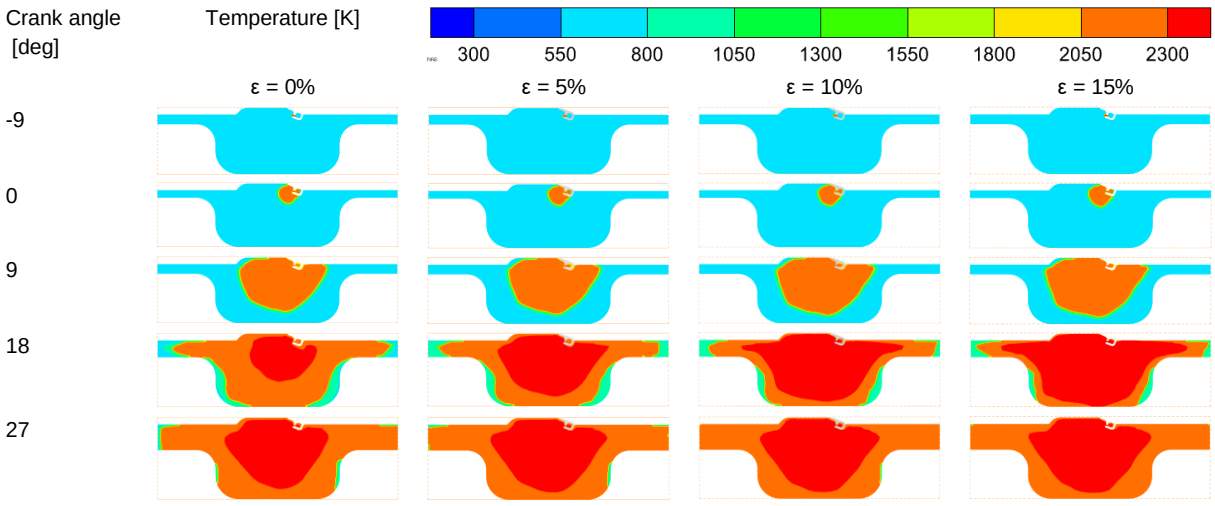

Figure 10. In-cylinder temperature distribution with syngas blending ration variation.

3.2 The Effect of Non-Standard Syngas Components on Methanol Engine Performance

Methanol reforming syngas primarily consists of H_2 and CO_2, with only trace amounts of CO. Therefore, when analyzing the effects of non-standard reformate gas compositions on methanol engine performance, only H_2 and CO_2 were considered. Additionally, a pure hydrogen composition was included to compare the differences between syngas and hydrogen. Selective catalytic oxidation and palladium membrane separators can effectively separate CO_2 from the syngas produced by methanol reforming, thereby obtaining high-concentration hydrogen[24]. Therefore, this study of non-standard reformate gas compositions was conducted at a blending ratio of ε =10%. The three non-standard reformate gas compositions are presented in Table 5.

Table 5. Configuration of non-standard syngas components.

Parameter	H_2 (%)	CO (%)	CO_2 (%)
H73	73	2	25
H83	83	2	15
H93	93	2	5
H100	100	0	0

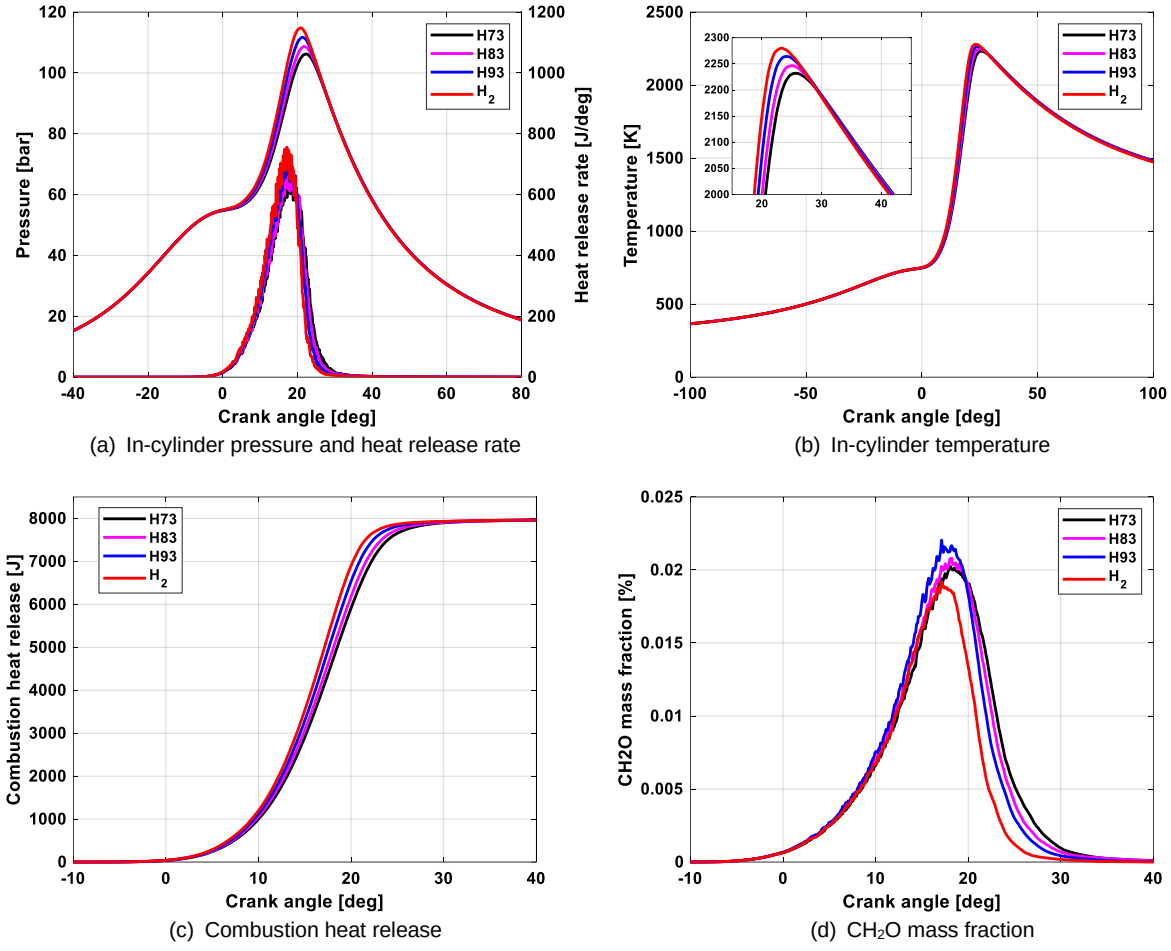

(a) In-cylinder pressure and heat release rate

(b) In-cylinder temperature

(c) Combustion heat release

(d) CH_2O mass fraction

Figure 11. Simulation results with syngas composition variation.

Figure 11 illustrates the effects of H73, H83, H93, and H100 syngas compositions on the combustion process of a spark-ignited methanol engine. From Figure 11(a), Figure 11(b), and Figure 11(c), it can be observed that increasing the hydrogen proportion in syngas enhances the heat release rate of the methanol engine, shortens the combustion duration, and further increases the peak in-cylinder pressure and in-cylinder temperature. Figure 11(d) presents the mass fraction variation of CH_2O radicals. The mass fraction of CH_2O radicals increases with a higher hydrogen ratio in the syngas, indicating that a higher hydrogen proportion promotes CH_2O radical formation, facilitating the oxidation reactions of methanol. However, when the syngas consists of pure hydrogen (H100), the CH_2O radical formation at the flame front significantly decreases, even

falling below that observed with the H73 syngas composition. This observation suggests that the mechanisms by which syngas and pure hydrogen promote methanol combustion are not entirely identical. To further explain this phenomenon, the in-cylinder formation process of CH_2O radicals is shown in Figure 12. With an increasing hydrogen proportion in syngas, the CH_2O radical formation during the early combustion phase (0°CA) becomes more pronounced. However, during the mid-to-late combustion phase (18°CA), the CH_2O radical formation decreases. Currently, the underlying reasons for this phenomenon remain unclear. Preliminary analysis suggests that CO and CO_2 in syngas may play a role in the intermediate reaction pathways of hydrogen and methanol combustion.

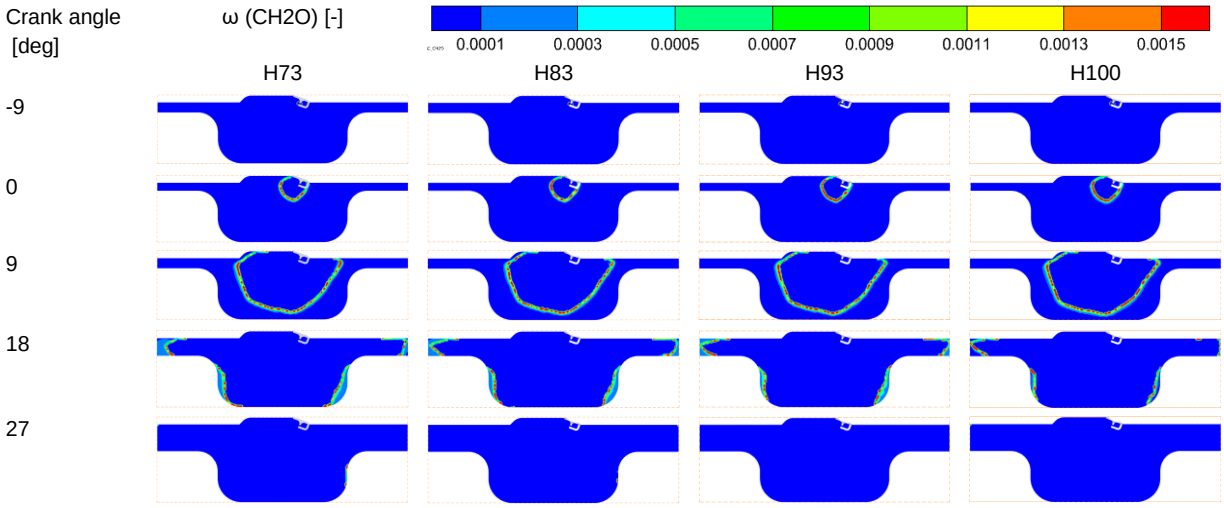

Figure 12. In-cylinder CH2O distribution with syngas composition variation.

Figure 13 illustrates the effects of increasing the hydrogen proportion in syngas on engine performance and emissions characteristics. Figure 13(a) shows the changes in the AFR and λ at the initial state of the in-cylinder mixture. As the CO_2 content in syngas decreases, more air can enter the cylinder, leading to an increase in both AFR and λ. Figure 13(b) displays the variation in KI and peak cylinder pressure. When the CO_2 content in syngas decreases from 0.25 to 0, the KI value increases from 1.63 bar to 4.12 bar, indicating that CO_2 effectively suppresses the knocking tendency and intensity in methanol engines. Figure 13(c) and Figure 13(d) show the changes in IMEP, BSFC, and specific emissions of NOx and CO_2 as syngas composition changes. When considering only direct carbon emissions from the methanol engine, a significant reduction in CO_2 specific emissions can be achieved. Similarly, the in-cylinder temperature distribution is analyzed to further discuss the formation of NOx and other emissions, as shown in Figure 14. Increasing the hydrogen content in the syngas results in higher overall combustion temperatures and a larger high-temperature region within the cylinder, leading to an increase in NOx formation.

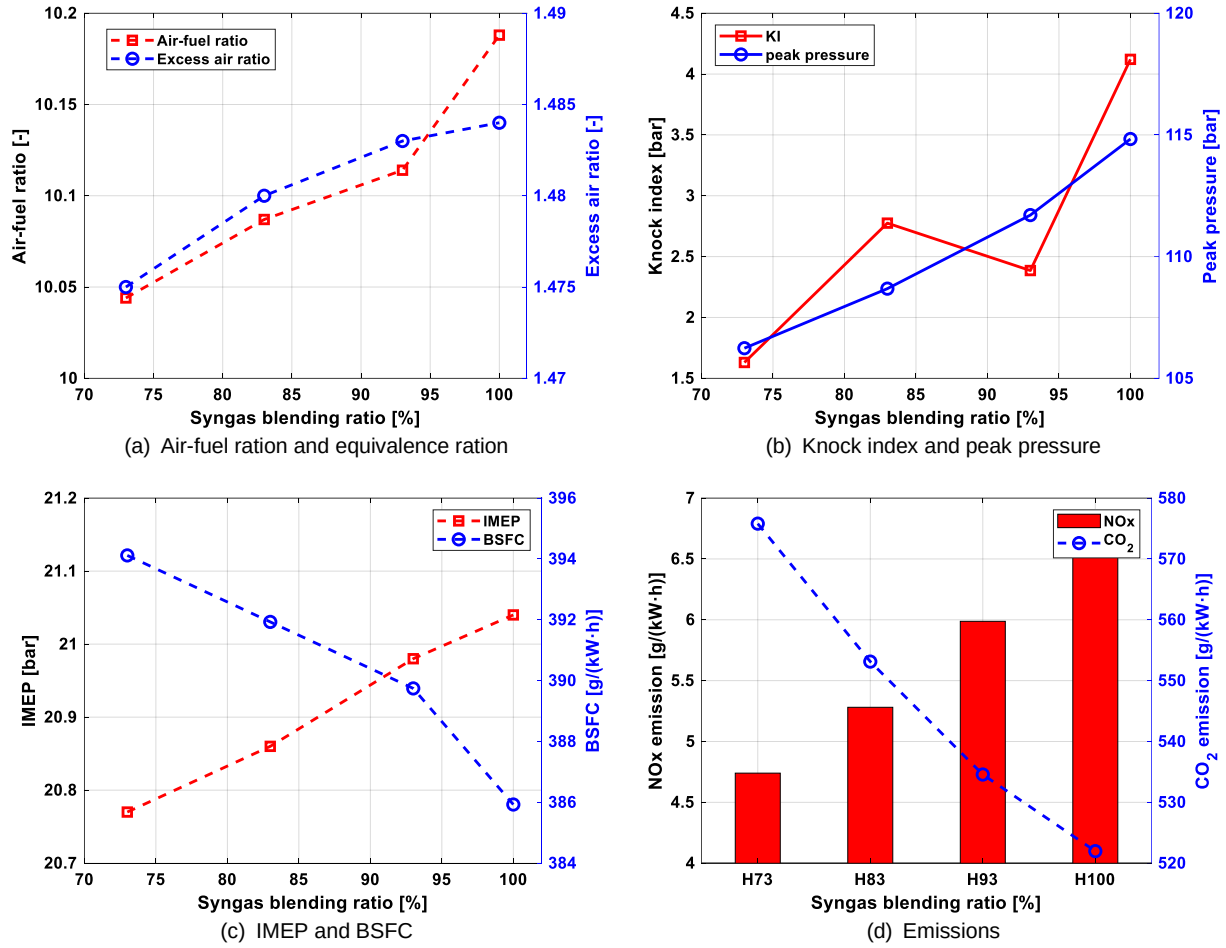

Figure 13. Simulation results with syngas composition variation.

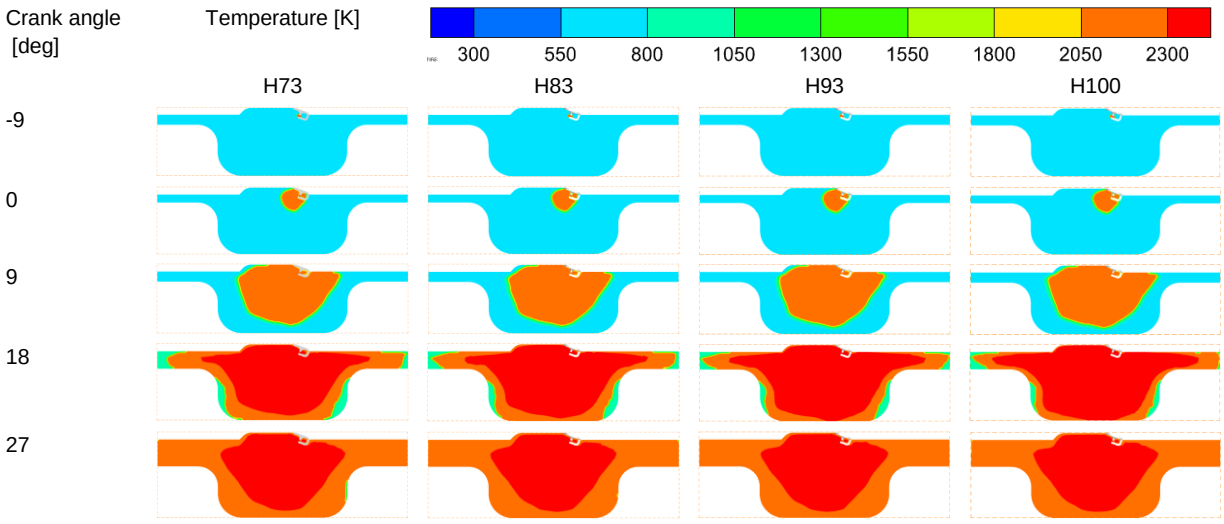

Figure 14. In-cylinder temperature distribution with syngas composition variation.

3.3 Parametric Investigation

To further reveal the impact of syngas, hydrogen, and syngas composition adjustment on the performance of a spark-ignited methanol engine, this study analyzed the effects of blending ratio and hydrogen proportion in syngas on BSFC, NOx emissions, and the KI, as shown in Figure 15. Figure 15(a) illustrates the effects of blending ratio and hydrogen proportion in syngas on BSFC, NOx emissions, and the KI at 100% load. The x-axis and y-axis represent BSFC and NOx specific emissions, respectively, while the color of the points indicates KI trends. The black arrows

represent the syngas blending ratio, ranging from 0% to 15% in 5% intervals. The blue line represents the effects of the standard syngas blending ratio on methanol engine performance, while the purple line represents the effects of pure hydrogen blending ratio on engine performance.

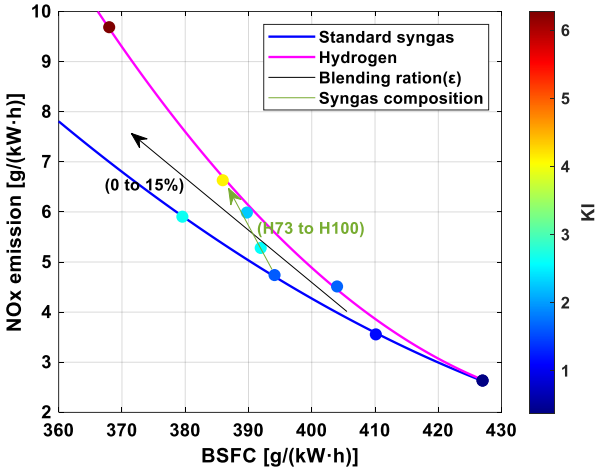

(a) 100% load (1500 r/min, 320 kW)

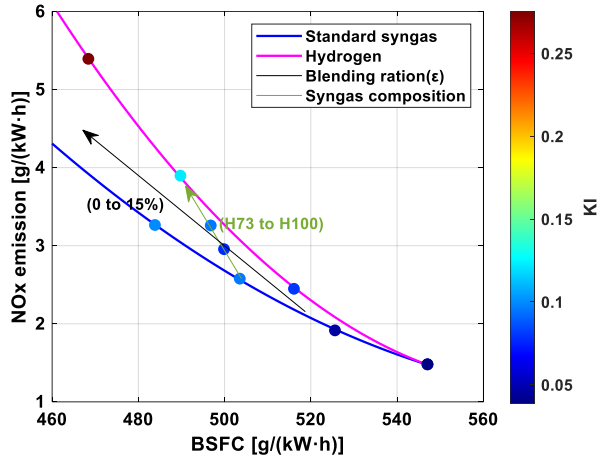

(b) 25% load (1500 r/min, 80 kW)

Figure 15. Comparison of BSFC, NOx emissions, and KI under different operation loads.

From Figure 15(a), it can be observed that increasing both the hydrogen and syngas blending ratios reduces the BSFC of the engine. However, this also significantly increases both the NOx specific emissions and the KI. Compared to pure hydrogen, syngas exhibits lower NOx emissions and a lower KI value at the same blending ratio. The green arrow in Figure 15(a) represents the performance of the methanol engine at a 10% blending ratio with different hydrogen proportions in the syngas. As the hydrogen proportion in syngas increases, the engine's BSFC and NOx emissions performance gradually approach those of pure hydrogen. However, the KI results do not exhibit complete consistency. Interestingly, at a 93% hydrogen volume fraction, the KI value is lower than those observed at 83% hydrogen volume fraction and even pure hydrogen.

Figure 15(b) illustrates the effects of blending ratio and hydrogen proportion in syngas on BSFC, NOx emissions, and the KI of a spark-ignited methanol engine under 25% load conditions. From Figure 15(b), it can be observed that the effects of syngas and hydrogen blending ratios on NOx emissions, BSFC, and KI follow a pattern similar to the 100% load condition. However, at 25% load, the maximum KI value is only 0.3 bar. From the perspective of knock intensity analysis, there is potential to further increase the syngas blending ratio under low-load conditions. Additionally, by adjusting the hydrogen proportion in the syngas composition, the engine's power performance and fuel economy can be further optimized.

4 CONCLUSIONS

In this study, a 3D CFD model of a spark-ignited methanol engine cylinder was developed and validated using the CONVERGE software. This model was employed to investigate the differences in the effects of methanol syngas and hydrogen on engine performance. Additionally, the study explored the influence of non-standard syngas compositions on methanol engine performance under both high-load and low-load conditions through composition adjustment. The main findings of this study are summarized as follows:

(a) The addition of syngas in a spark-ignited methanol engine increases the methanol combustion speed and shortens the duration of the heat release rate. Furthermore, syngas addition significantly enhances the formation of CH_2O radicals. However, as the syngas blending ratio increases, the growth rate of CH_2O radical mass fraction gradually slows down, indicating that the components in syngas can induce or promote methanol oxidation reactions, but this promotion effect plateaus beyond a certain blending ratio threshold.

(b) Increasing the hydrogen proportion in standard syngas further enhances the methanol engine's heat release rate and shortens the combustion duration. The mass fraction of CH_2O radicals increases with a higher hydrogen proportion in syngas, indicating that a higher hydrogen content promotes CH_2O radical formation, facilitating the methanol oxidation reaction. However, when the syngas consists solely of hydrogen, the CH_2O radical formation at the flame front

significantly decreases, even falling below that observed with H73 syngas composition. This finding suggests that the mechanisms by which syngas and hydrogen promote methanol combustion are not entirely identical.

(c) Increasing the blending ratio of hydrogen and syngas effectively reduces the BSFC of the methanol engine. However, both NOx specific emissions and the KI increase significantly. Compared to pure hydrogen, at the same blending ratio, syngas exhibits lower NOx emissions and a lower KI value. Under 25% load conditions, the influence of hydrogen and syngas blending on NOx emissions, BSFC, and KI follows a pattern similar to that observed under 100% load conditions. However, at 25% load, the maximum KI value reaches only 0.3 bar. From the perspective of knock intensity analysis, there is potential to further increase the syngas blending ratio under low-load conditions. Additionally, by adjusting the hydrogen proportion in syngas, the engine's power performance and fuel economy can be further optimized.

This study contributes to a deeper understanding of the combustion characteristics, emission formation, and knock occurrence in spark-ignition methanol engines after syngas blending. The results provide valuable insights into the application of methanol reforming syngas in methanol engines, offering a guidance for the application of on-board methanol-reforming technology in maritime vessels.

5 DEFINITIONS, ACRONYMS, ABBREVIATIONS

AFR:	Air-Fuel Ratio
AMR:	Adaptive Mesh Refinement
BSFC:	Brake Specific Fuel Consumption
CA:	Crank Angle
CCD:	Central Composite Design
EGR:	Exhaust Gas Recirculation
Error.exp	Relative error relative to the experimental values
EVO:	Exhaust Valve Opening
IMEP:	Indicated Mean Effective Pressure
IVC:	Intake Valve Closure
KI:	Knock Index
LHV:	Lower Heating Value
MSR:	Methanol Steam Reforming
NOx:	Nitrogen Oxides
TDC:	Top Dead Center
D:	Mass diffusion coefficient
e:	Specific internal energy
h:	Enthalpy
K:	Thermal conductivity
p:	Pressure
p_{max}:	Peak pressure
$PP_{max,n}$:	Maximum absolute difference of the band-pass filtered pressure
R:	Gas constant
S:	Source term
T:	Temperature
u:	Velocity
V:	Volume
λ:	Excess air ratio
ε:	Energy blending ratio of syngas
ρ:	Density
σ_{ij}:	Stress tensor
γ_m:	Mass fraction of species

6 REFERENCES AND BIBLIOGRAPHY

[1] Duan X, Chu X, Wang R, Chen Z, Zhou F, Abdellatief TMM. 2024. The performance and emissions characteristics of the gasoline spark ignition engine fuelled with green and renewable methanol and hydrogen. *Renew Energy*. 240: 122184.

[2] Yang R, Liu Z, Liu J. 2024. The methodology of decoupling fuel and thermal nitrogen oxides in multi-dimensional computational fluid dynamics combustion simulation of ammonia-hydrogen spark ignition engines. *Int J Hydrogen Energy*. 55:300–318.

[3] Duan H, Hu W, Wang J, Yin X, Hu E, Zeng K. 2025. Effects of diesel pilot-injection strategy on a methanol/diesel dual-direct injection engine. *Applied Thermal Engineering*. 261:125106.

[4] Costantini MG. 1993. Health effects of oxygenated fuels. *Environmental Health Perspectives*. 101: 151–160.

[5] Karvounis P, Theotokatos G, Patil C, Xiang L, Ding Y. 2025. Parametric investigation of

diesel–methanol dual fuel marine engines with port and direct injection. *Fuel*. 381: 133441.

[6] Wei Y, Zhu Z, Liao Y, Liu S, Shi Z, Zeng Z, et al. 2023. Numerical investigations on the effects of EGR routes on the combustion characteristics and efficiency of a heavy-duty SI methanol engine. *Fuel Processing Technology*. 250:107861.

[7] Feng H, Lai K, Zheng Z, Lin S, Wu X, Tang Q. 2024. Effects of methanol direct injection and high compression ratio on improving the performances of a spark-ignition passenger car engine. *Fuel*. 357:130052.

[8] Zhang B, Ji C, Wang S, Zhou X. 2014. Idling Performance of a Hydrogen-blended Methanol Engine at Lean Conditions. *Energy Procedia*. 61:331–334.

[9] Zhang B, Ji C, Wang S, Xiao Y. 2014. Investigation on the cold start characteristics of a hydrogen-enriched methanol engine. *International Journal of Hydrogen Energy*. 39:14466–14471.

[10] Liu H, Yang Y, Zhou Z, Baig A, Liu S, Zhu Z, et al. 2025. Numerical investigation on the efficiency improvement and knock mitigation through combustion chamber optimization in a heavy-duty spark-ignition methanol engine with EGR. *Applied Thermal Engineering*. 264:125469.

[11] Suijs W, Dierickx J, Pu Y-H, Wang Y, Verhelst S. 2024. Calibrating the Livengood–Wu integral knock model for differently sized methanol engines. *Fuel Communications*. 19:100121.

[12] Zhang B, Ji C, Wang S. 2015. Combustion analysis and emissions characteristics of a hydrogen-blended methanol engine at various spark timings. *International Journal of Hydrogen Energy.* 40:4707–4716.

[13] Ma F, Ding S, Wang Y, Wang Y, Wang J, Zhao S. 2008. Study on combustion behaviors and cycle-by-cycle variations in a turbocharged lean burn natural gas S.I. engine with hydrogen enrichment. *International Journal of Hydrogen Energy*. 33:7245–55.

[14] Iyer SN, Rrustemi DN, Ganippa LC, Megaritis T. 2024. Hydrogen enrichment in methanol SI engine at varying injection timing during compression stroke. *International Journal of Hydrogen Energy*. 89:952–963.

[15] Tian Z, Wang Y, Zhen X, Liu D. 2022. Numerical comparative analysis on performance and emission characteristics of methanol/hydrogen, ethanol/hydrogen and butanol/hydrogen blends fuels under lean burn conditions in SI engine. *Fuel*. 313: 123012.

[16] Gong C, Li Z, Yi L, Huang K, Liu F. 2020. Research on the performance of a hydrogen/methanol dual-injection assisted spark-ignition engine using late-injection strategy for methanol. *Fuel*. 260:116403.

[17] Liao C-H, Horng R-F. 2016. Investigation on the hydrogen production by methanol steam reforming with engine exhaust heat recovery strategy. *International Journal of Hydrogen Energy.* 41:4957–4968.

[18] Srivastava A, Kumar P, Dhar A. 2021. A numerical study on methanol steam reforming reactor utilizing engine exhaust heat for hydrogen generation. *International Journal of Hydrogen Energy*. 46:38073–38088.

[19] Zhan H, Li S, Yin G, Gao Y, Hu E, Huang Z. 2023. Experimental and kinetic study of methanol reforming and methanol-syngas co-oxidation at high pressure. *Fuel Processing Technology*. 252:107944.

[20] Wang Y, Long W, Tian H, Dong P, Lu M, Tang Y, et al. 2024. Research on oxidation mechanism of hydrogen/syngas-methanol and its application on engine performance prediction. *Fuel*. 365:131211.

[21] Xiang L, Theotokatos G, Ding Y. 2023. Parametric investigation on the performance-emissions trade-off and knocking occurrence of dual fuel engines using CFD. *Fuel*. 340:127535.

[22] Horvath AL. 1974. Redlich-Kwong equation of state: review for chemical engineering calculations. *Chemical Engineering Science*. 29:1334–1340.

[23] Zhu L, Li B, Li A, Ji W, Qian Y, Lu X, et al. 2020. Effects of fuel reforming on large-bore low-speed two-stroke dual fuel marine engine combined with EGR and injection strategy. *International Journal of Hydrogen Energy*. 45:29505–17.

[24] Zhou S, Xie Z, Sun Y, Jin J, Zhang Y, Pei F. 2021. Modeling and Hydrogen Supply Management of a Vehicle Onboard Methanol Reforming Fuel Cell System. *JOURNAL OF TONGJI UNIVERSIT*. 49:1596–605.